

# VLBA Measurement of Nine Pulsar Parallaxes

Walter F. Brisken

*National Radio Astronomy Observatory*

*PO Box O, Socorro, NM 87801*

wbrisken@nrao.edu

John M. Benson

*National Radio Astronomy Observatory*

*PO Box O, Socorro, NM 87801*

jbenson@nrao.edu

W. M. Goss

*National Radio Astronomy Observatory*

*PO Box O, Socorro, NM 87801*

mgoss@nrao.edu

and

S. E. Thorsett

*Department of Astronomy and Astrophysics, University of California*

*Santa Cruz, CA 95064*

thorsett@ucolick.org

## ABSTRACT

We determined the distances to nine pulsars by parallax measurements using the NRAO Very Long Baseline Array, doubling the number of pulsars with accurate distance measurements. Broadband phase modeling was used to calibrate the varying dispersive effects of the ionosphere and remove the resulting phase errors from the phase-referenced VLBI data. The resulting parallaxes have a typical accuracy of 100 microarcseconds or better, yielding distances measurements as accurate as 2%. We also report new proper motion measurements of these pulsars, accurate to  $400 \mu\text{as yr}^{-1}$  or better.

*Subject headings:* astrometry — techniques: interferometric — pulsars

## 1. Introduction

Accurate pulsar distance measurements are useful for many reasons. Combined with dispersion measures, they probe the electron content along different lines of sight through the local Galaxy. Combined with proper motions, they constrain the pulsar velocity distribution and hence the symmetry of supernova explosions. Combined with radio, optical, x ray, and UV flux measurements, they determine the absolute luminosities and radiation efficiencies of pulsars. For a thermally emitting neutron star, they even promise the possibility of directly constraining the neutron star radius and hence the nuclear equation of state at high densities. There are many different ways of estimating pulsar distances, including association with supernova remnants or globular clusters at known distance, or the use of a model of the electron distribution in the Galaxy together with dispersion measurements. But the most fundamental method—indeed, the only model-independent method—remains the measurement of parallaxes.

Pulsar parallax measurements are difficult. Even the closest pulsars are 100 pc or more distant; thus parallax leads to an apparent annual motion of 10 mas or (typically) much less. With their steep spectra, pulsars are usually observable only in the low-frequency radio band, where the ionosphere introduces substantial temporally- and geographically-variable shifts in the phase of the signal, making precision interferometry particularly challenging.

Before the completion of the Very Long Baseline Array (VLBA), only six interferometric pulsar parallaxes were published (Table 1). It is important to understand the very great difficulties these observers faced. First, in many cases they were limited to rather short baselines ( $< 500$  km) and decimeter and longer wavelengths ( $\lambda > 10$  cm). The ionosphere and the small array size limited the potential accuracy to about 1 milliarcsecond (mas), unless a very nearby calibrator source was used. Some serendipitous measurements were possible. For example, the measurement of the parallax of pulsar B1451–68 was about ten times more precise than the ionosphere would ordinarily have allowed with the available array because of the fortuitous presence of a calibrator only  $6'$  from the pulsar, within the same primary telescope beam.

A second problem for early observers was the limited number of telescopes available in early, ad hoc VLBI networks. With only three or fewer stations, it is very difficult to fully resolve “phase-wrap” ambiguities to determine which of a family of possible positions on the sky is actually occupied by the source. As shown in Brisken *et al.* (2000), an incorrect choice of phase wraps could lead to parallax errors much larger than the formal measurement errors. (By the time the last measurement in Table 1 was made—the parallax of B2021+51—a number of VLBA stations was available. Although the observations used a different set of telescopes at each observing epoch, and large baseline errors in the telescope

positions had still not been resolved, it is notable that this early result is within  $2\sigma$  of our new measurement.) It is probably not coincidental that every repeated pulsar parallax measurement has yielded a smaller parallax (and greater pulsar distance). We suspect that the expectation of larger results in early experiments probably contributed to incorrect lobe choices. With the ten-station VLBA this is no longer a problem.

Although we will not further discuss non-radio measurements here, for completeness we note that the high-energy pulsar Geminga (J0633+1746) has a three-epoch parallax measured by HST of  $\pi = 6 \pm 2$  mas (Caraveo et al., 1996), and the radio quiet neutron star J185635–3754 has an HST-derived parallax of  $16.5 \pm 2.3$  mas (Walter, 2001).

Table 1. Early interferometric pulsar parallaxes

Pulsar	Stations	Baseline (km)	$\nu_{\text{obs}}$ (MHz)	epochs	$\pi$ (mas)	Reference
B0823+26	3	5300	1660	4	$2.8 \pm 0.6$	1
B0950+08	3	5300	1660	4	$7.9 \pm 0.8$	1
B1451-68	2	275	1600	9	$2.2 \pm 0.3$	2
B1929+10	2	127	480	$\sim 7$	$21.5 \pm 8.0$	3
B1929+10	4	35	2695	5	$< 4$	4
B2021+51	4–6	$\sim 6000$	2218	4	$0.95 \pm 0.37$	5

References. — (1) Gwinn et al., 1986; (2) Bailes et al., 1990; (3) Salter et al., 1979; (4) Backer & Sramek, 1982; (5) Campbell et al., 1996

## 2. Objectives and Target Selection

Our successful measurement (Briskin et al. 2000) of the parallax of PSR B0950+08, using a new calibration technique to remove the disruptive effects of the ionosphere from the interferometry data, prompted us to expand our program of parallax measurements to a larger sample. We had two primary goals. One was the immediate desire to increase the number of pulsars with well-measured distances. But a second goal was to improve our understanding of the new calibration technique, to test its limitations, and to measure the level of residual systematic errors. For this reason, our target selection was not yet optimized solely to produce an unbiased pulsar sample for statistical work on pulsar distances. Instead, we chose nine pulsars at a variety of declinations, of varying flux densities, and with varying pulsar-calibrator angular separations. We also continued our observations of PSR B0950+08, to produce an extremely over-constrained data set for studies of our errors.

An important constraint on target selection was the need for a high flux density at 1400 MHz. Based on our experience with B0950+08, we expected that we would be able to successfully do an ionospheric correction for pulsars with flux densities above about 10 mJy at 1400 MHz. We also preferentially targeted pulsars with estimated distances (from the dispersion model) of less than about 2 kpc. For this experiment, we only considered candidate pulsars whose nearest VLBA calibrator source was no more than  $5^\circ$  from the pulsar. Larger separations lead to larger differential ionospheric and tropospheric effects, and will be more difficult to calibrate. The  $5^\circ$  limit was set after experiments in which we attempted to calibrate PSR B0950+08 against the International Celestial Reference Frame calibrator source 1004+141, at a separation of  $6.9^\circ$ . At this separation the differential propagation effects were too large to correct using the new calibration technique. We also rejected pulsars at declinations below  $-10^\circ$ , where high elevation ( $> 20^\circ$ ) observations cannot be made simultaneously at all VLBA stations. The pulsars observed are listed in Table 2, together with their dispersion measures and flux densities from the Princeton pulsar catalog (Taylor et al., 1993).

Table 2. Pulsars observed

Pulsar	DM (pc cm <sup>-3</sup> )	$S_{1400}$ (mJy)	Gate gain <sup>†</sup> (mJy)	Calibrator	$\theta_{\text{sep}}$
B0329+54	26.776	203	4.08	J0302+5331	4°37′
B0809+74	5.7513	10	3.27	J0808+7315	1°19′
B0950+08	2.9702	84	3.09	J0946+1017	2°52′
B1133+16	4.8471	32	5.98	J1143+1834	3°15′
B1237+25 <sup>‡</sup>	9.2755	20	5.13	J1240+2405	0°51′
				J1230+2518	2°11′
B1929+10	3.176	41	4.03	J1945+0952	2°20′
B2016+28	14.176	30	4.99	J2020+2826	0°38′
B2020+28	24.62	38	4.69	J2020+2826	0°36′
B2021+51	22.580	27	4.90	J2025+5028	1°30′
J2145−0750	9.000	10	1.91	J2142−0437	3°18′

<sup>†</sup>The improvement in signal-to-noise by not correlating during off-pulse.

<sup>‡</sup>B1237+25 was observed with two reference sources.

Table 3. Calibrator positions and flux densities<sup>a</sup>

Name	$\alpha(\text{J2000})^b$	$\delta(\text{J2000})$	$S_{2267}^c$ (mJy)	$S_{8337}^d$ (mJy)
J0302+5331	03 <sup>h</sup> 02 <sup>m</sup> 22 <sup>s</sup> .7354	53°31′46″.534	200	192
J0808+7315	08 <sup>h</sup> 08 <sup>m</sup> 16 <sup>s</sup> .4918	73°15′11″.980	220	269
J0946+1017	09 <sup>h</sup> 46 <sup>m</sup> 35 <sup>s</sup> .0693	10°17′06″.126	390	248
J1143+1834	11 <sup>h</sup> 43 <sup>m</sup> 26 <sup>s</sup> .0706	18°34′38″.375	230	113
J1230+2518	12 <sup>h</sup> 30 <sup>m</sup> 14 <sup>s</sup> .0912	25°18′07″.139	150	175
J1240+2405	12 <sup>h</sup> 40 <sup>m</sup> 47 <sup>s</sup> .9870	24°05′14″.184	160	92
J1945+0952	19 <sup>h</sup> 45 <sup>m</sup> 15 <sup>s</sup> .9229	09°52′59″.576	250	198
J2020+2826	20 <sup>h</sup> 20 <sup>m</sup> 45 <sup>s</sup> .8719	28°26′59″.205	90	18
J2025+5028	20 <sup>h</sup> 25 <sup>m</sup> 24 <sup>s</sup> .9726	50°28′39″.550	280	165
J2142−0437	21 <sup>h</sup> 42 <sup>m</sup> 36 <sup>s</sup> .8999	−04°37′43″.518	65	33

<sup>a</sup>All values listed are from the VLBA Calibrator List (Beasley et al., 2002).

<sup>b</sup>Source positions are accurate to 15 mas. Better positions for some of these calibrators are now known.

<sup>c</sup>Correlated flux density on 8000 km baseline at 2267 MHz.

<sup>d</sup>Peak source brightness of VLBA image made at 8337 MHz.

### 3. Observations

Five epochs of observations for each pulsar were planned over the course of one year, enough to redundantly determine the proper motion and parallax even with a failed epoch. To maximize our sensitivity to the angular signature of parallax, the measurements were scheduled at times when the parallactic displacement was at a maximum or minimum. Observations hence occurred at roughly three month intervals, although the exact dates varied with telescope scheduling. Pulsar J2145–0750 was not detected in either of its first two epochs. This non-detection is most likely because of the extreme, long-term scintillation modulation that affects the signal from this pulsar. It was dropped from the program, and the time allotted to other pulsars was increased slightly. About ninety minutes of on-source integration was obtained for each pulsar at each epoch.

In order to make relative position measurements, each pulsar observation was interleaved with observations of a VLBA calibrator source with position known to better than 15 mas. The antennas nodded back and forth between the pulsar and calibrator with a cycle time of about five minutes. This interval is long enough to detect calibrator fringes yet short enough to allow unambiguous phase connection between calibrator observations. In the case of B1237+25 two calibrators were observed in a cycle, integrating for 100 seconds on the pulsar and 60 seconds on each calibrator.

All observations were made with the ten-station NRAO VLBA. The 20 cm band (1400 to 1740 MHz) was chosen as a compromise between falling flux densities and increasing resolution as frequency increases. This band also offers the wide fractional bandwidths needed for the ionosphere calibration. The 338 MHz wide band available from the receivers was Nyquist sampled in eight 8 MHz spectral windows beginning at 1404, 1414, 1434, 1474, 1634, 1694, 1724 and 1734 MHz. Pulsar gating was employed to increase the signal-to-noise of the pulsar measurements by disabling correlation during off-pulse. The gate gain listed in Table 2 is the expected signal-to-noise increase factor based on the pulse profiles measured at 1400 MHz. The timing data needed to construct the pulse arrival time ephemerides was collected by Andrew Lyne at Jodrell Bank.

## 4. Data Reduction

### 4.1. Calibration

Data reduction was performed with the AIPS software package. Phase-referencing (Shapiro et al. 1979) was used to relate the pulsar’s position to that of its calibrator.



Corrections for the structure of the calibrator source were made. The absolute position shift caused by structure is less than 1 mas for most VLBA calibrators. Epoch-to-epoch position shift caused by differences in the baseline coverage is a smaller effect but is more important for relative astrometry. Phase-referencing cancels out most of the pulsar’s phase errors such as those due to clock and baseline offsets and bulk propagation effects; however, propagation effects that are path-dependent are not exactly cancelled and dominate the remaining phase errors. At 20 cm, the largest of these effects is due to the ionosphere. A technique for removing the effect of the ionosphere without independent calibration information was described by Briskin et al. (2000). It is briefly described here.

The phase shift at frequency  $\nu$  due to a free electron column density of  $\sigma_{e^-}$  is

$$\Delta\phi_{\nu}^{\text{Iono}} \propto \frac{\sigma_{e^-}}{\nu}. \quad (1)$$

The wet troposphere also causes phase shifts, but with a non-dispersive dependence on  $\nu$ ,

$$\Delta\phi_{\nu}^{\text{Tropo}} \propto \sigma_{\text{H}_2\text{O}} \nu, \quad (2)$$

where  $\sigma_{\text{H}_2\text{O}}$  is the column density of water in the atmosphere. Only the differential phase shifts at two antennas enter into the visibility phases. After phase-referencing, only the difference in visibility phase shifts due to propagation between the pulsar and calibrator remain. While the absolute phase shifts may be several thousand degrees, only the double-differences of their values are relevant to the position measurements. For the troposphere, we find that this amount is typically less than  $45^\circ$  of phase for calibrator-target separations of up to  $5^\circ$  at 20 cm. In contrast, the differential ionosphere can be up to  $1200^\circ$  on long baselines.

In addition to the unwanted phase shifts due to propagation effects, the geometric phase associated with the position of the pulsar (the quantity that is to be determined) also contributes to the pulsar’s visibility phase. The point-like nature of pulsars simplifies the geometric phase to

$$\phi_{\nu}^{\text{Geom}} = \frac{\nu}{c}(\ell u + m v), \quad (3)$$

where  $(\ell, m)$  are the pulsar’s offset from the correlation center in radians,  $c$  is the speed of light, and  $(u, v)$  are the components of the projected baseline perpendicular to the direction to the pulsar. The phase delays due to geometry and the troposphere are both independent of frequency (non-dispersive), making their disentanglement impossible for a given visibility. Visibility measurements spanning a large range of elevations can be used to separate out the troposphere, but this was not done due to the limited elevation ranges that we used. Fortunately, it is possible to measure the differential ionosphere strength with multi-frequency

data since the ionosphere’s phase delay is frequency dependent (dispersive). The visibility phase on a single baseline can be expressed as

$$\phi_{\nu}^{\text{Vis}} = A\nu + \frac{B}{\nu} + 2\pi n. \quad (4)$$

where  $A$  incorporates all of the non-dispersive components (the geometry and the troposphere),  $B$  is the strength of the differential ionosphere, and the integer  $n$  is the number of additional phase wraps. Once  $B$  is known, the distorting effects due to the ionosphere can be removed from the visibility.

Station-based ionosphere solutions were determined by fitting station-based phases to Eqn 4. The station-based phases at each frequency band were determined by fitting the measured phases to a point source model representing the pulsar with solution intervals shorter than the amount of time that the ionospheric phase shift changes by about  $30^\circ$  (about 20 or 30 seconds at 20 cm). Solution intervals of 10 seconds or less were used on the brightest pulsars. Since all phases are relative, one station was chosen to be the reference antenna and was assigned zero phase.

Unknown phase wraps complicate the fitting for  $A$  and  $B$ . This is because certain combinations of the  $A$  and  $B$  parameters closely mimic an additional undetectable phase wrap due to the limited spanned bandwidth as is shown in Figure 1. The fitting was performed first on the Southwestern Antennas (Fort Davis, TX, Kitt Peak, AZ, Los Alamos, NM, and Pie Town, NM) where baselines are shorter and thus the geometric phases are smaller and the differential propagation effects are also less. An image was made without any ionosphere calibration to determine the pulsar’s position to better than 10 mas. The pulsar’s approximate position was used to reduce the unknown non-dispersive phase to less than  $90^\circ$ . Since the tropospheric phase is usually less than  $45^\circ$ , the number of phase shifts,  $n$ , can be determined and the ionosphere can be calibrated away for the Southwestern antennas. The phase shifts associated with the fitted  $B$  parameters were removed from the visibility data. An image made with the ionosphere calibrated Southwestern antennas yielded pulsar positions to better than 1 mas, allowing ionosphere solutions to be found at and applied to the remaining stations.

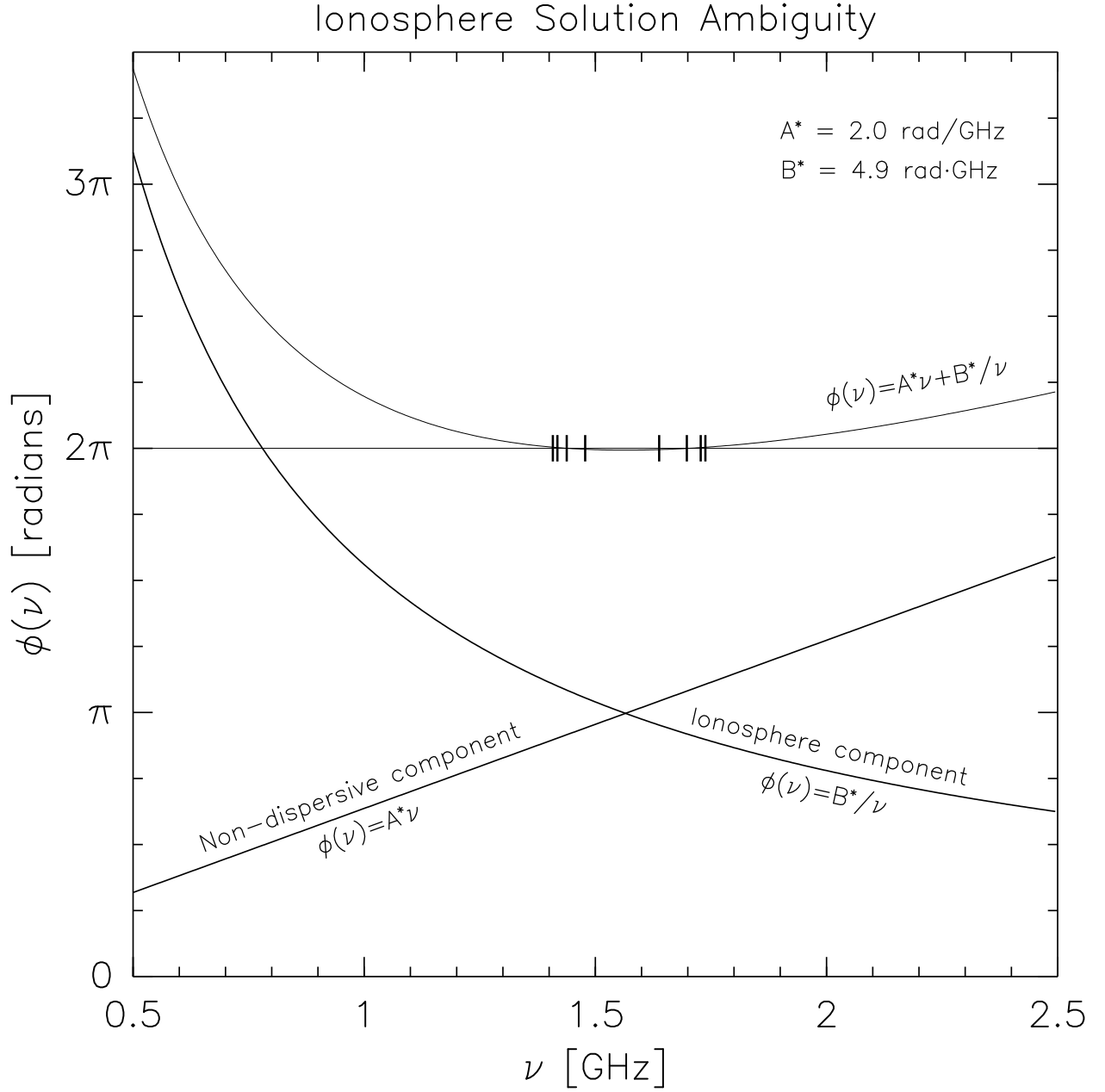


Fig. 1.— The source of phase-wrap ambiguity. For certain ionosphere solutions,  $A^* = 2.0 \text{ rad/GHz}$  and  $B^* = 4.9 \text{ rad}\cdot\text{GHz}$ , the resultant phase across the observed band is almost indistinguishable from  $2\pi$ . Since  $2\pi$  can be added to the visibility phases without observable consequences, an entire family of ionosphere solutions is consistent with the data. The eight 8 MHz bands observed are shown as short vertical bars. The RMS deviation from  $2\pi$  at these frequencies is only  $0.6^\circ$ .

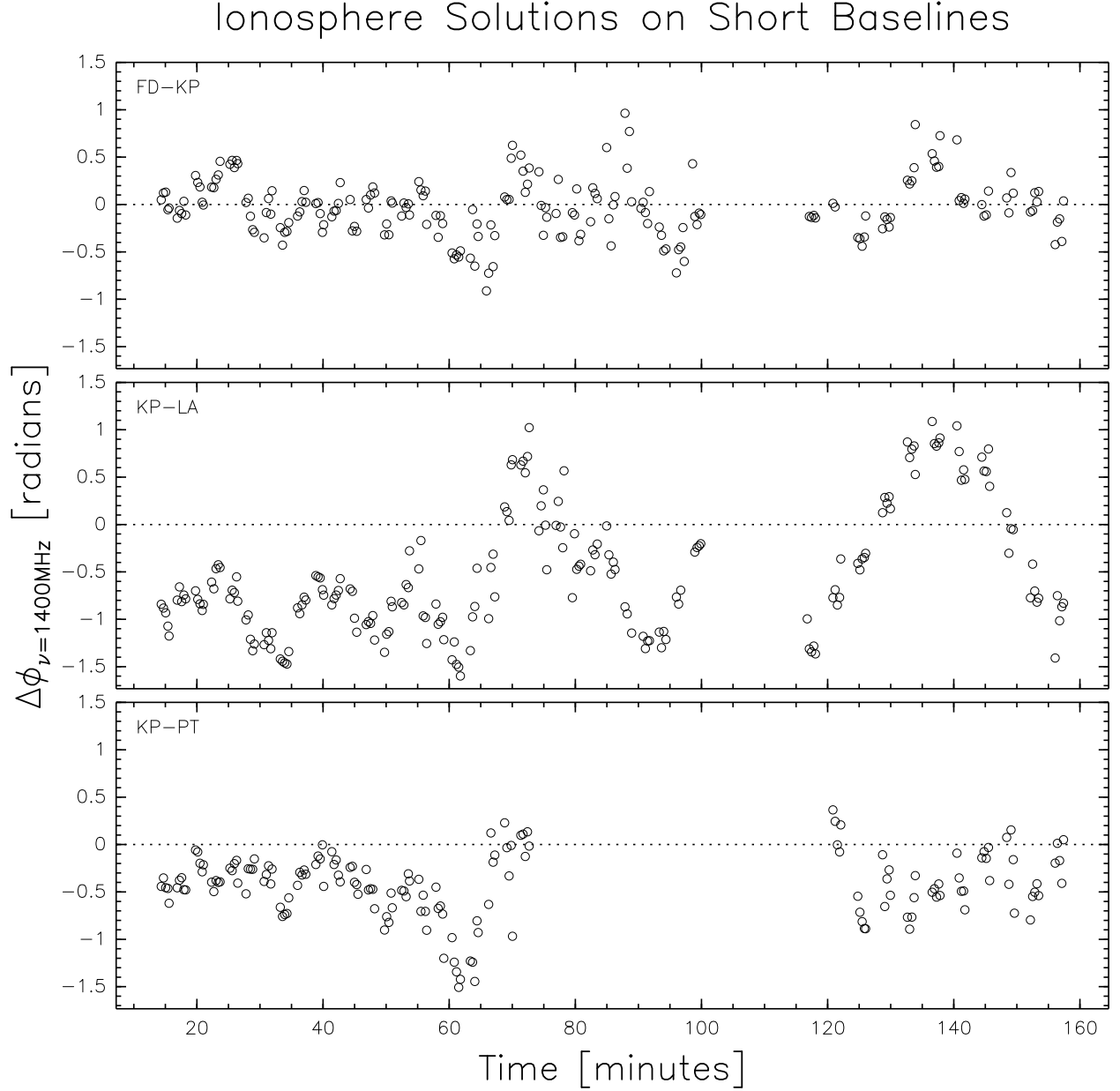


Fig. 2.— The relative phase due to the different residual ionospheric content above two antennas that is left uncalibrated by phase-referencing. Kitt Peak (KP) was used as the reference antenna in this observation. The three shortest baselines to Kitt Peak are shown above. Distances are: Fort Davis (FD) to KP = 744 km, KP to Los Alamos (LA) = 652 km, and KP to Pie Town (PT) = 417 km. These solutions are from the phase-referencing of PSR B1929+10 via calibrator J1945+0952, a separation of  $2^{\circ}20'$ . The gap in the data between 100 and 115 minutes is due to the observation of the bandpass calibrator. The larger gap on the KP–PT baseline is due to telescope failure at PT. The date of this observation was 1999 November 16.

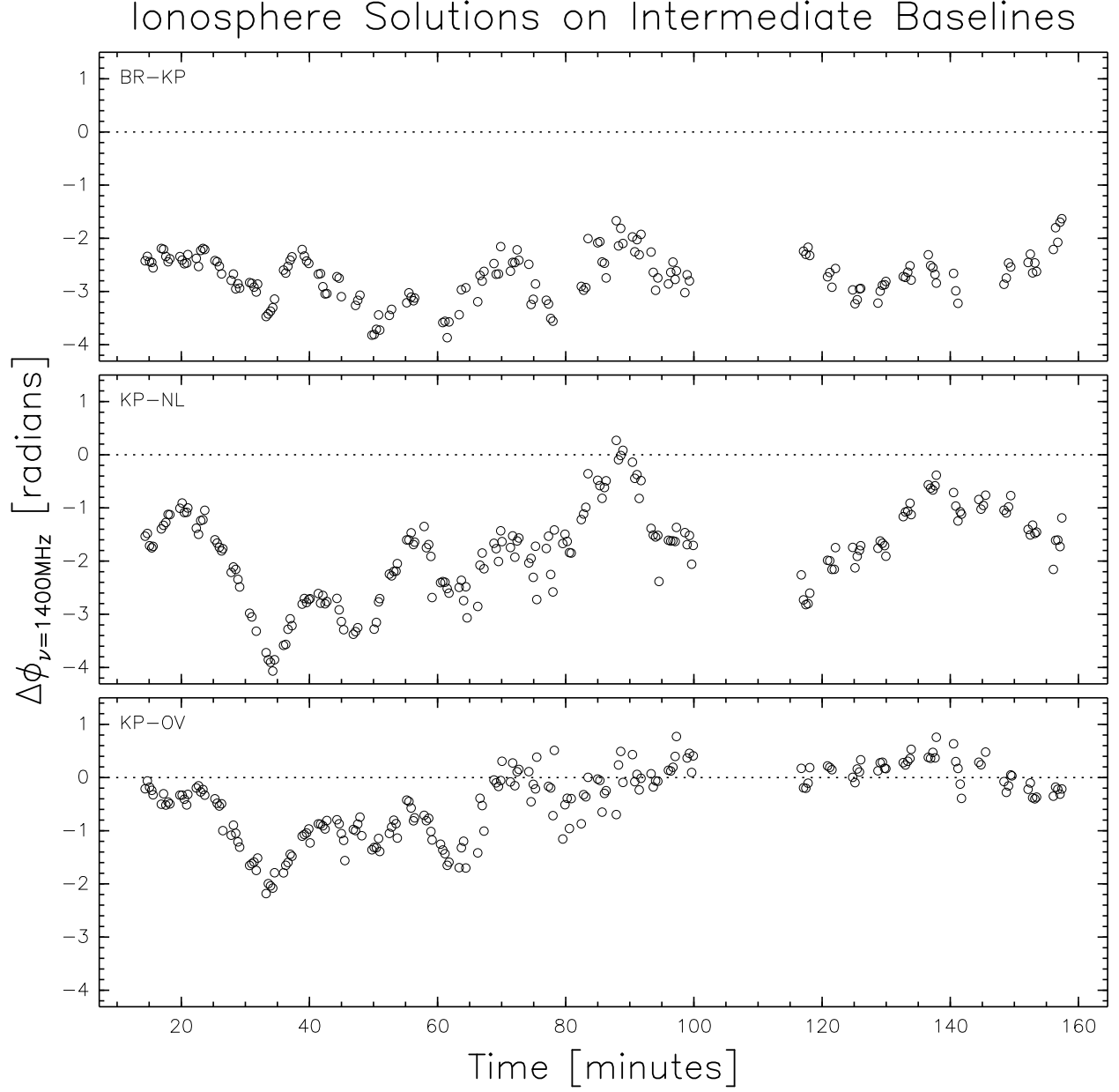


Fig. 3.— Same as Figure 2 but on the three intermediate length baselines to Kitt Peak. Distances are: Brewster (BR) to KP = 1913 km, KP to North Liberty (NL) = 2075 km, and KP to Owens Valley (OV) = 845 km. The bias in each frame is due to systematic differences in the line-of-sight electron density at the two stations.

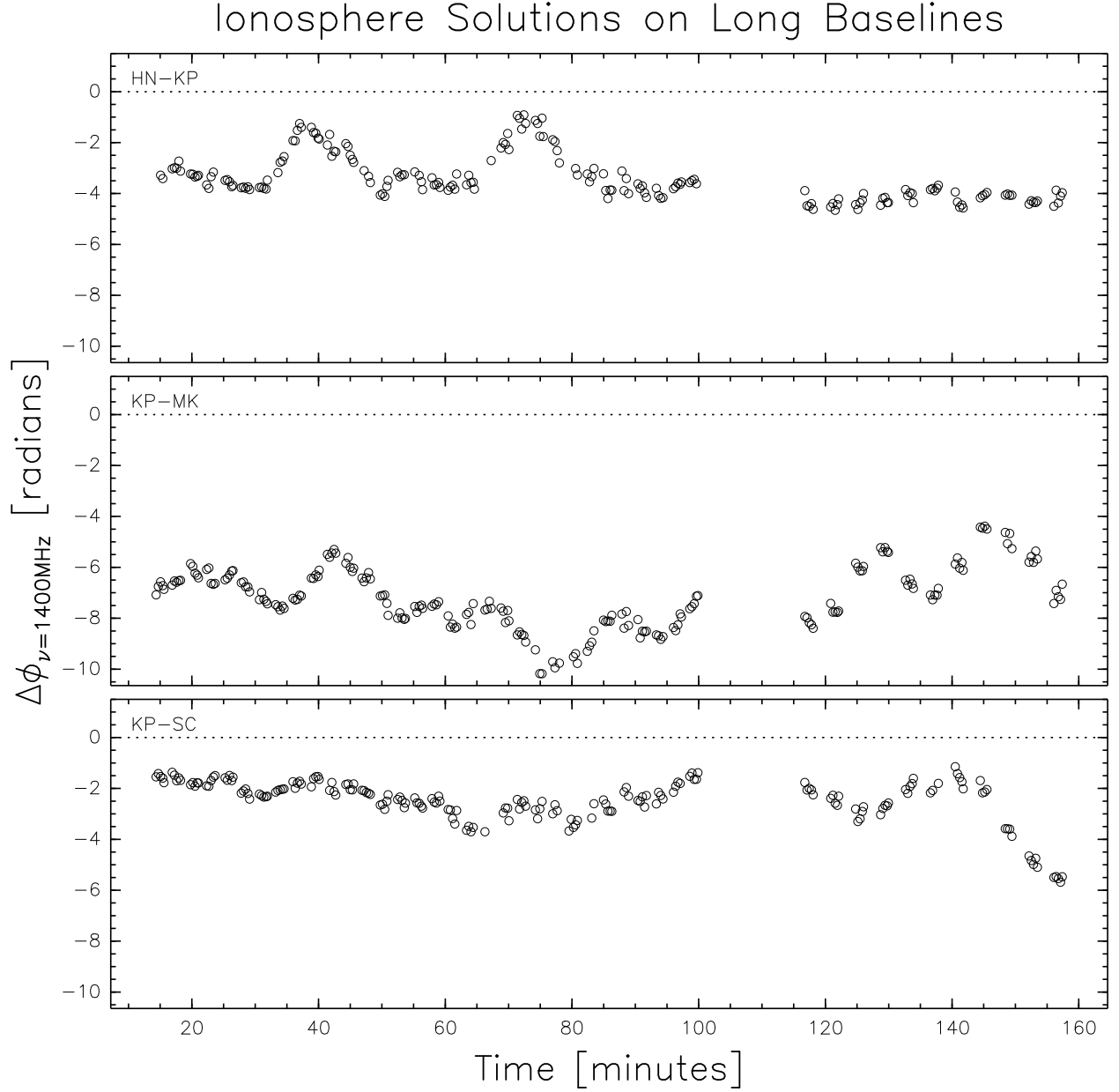


Fig. 4.— Same as Figures 2 and 3, but on the three longest baselines to Kitt Peak. Distances are: Hancock (HN) to KP = 3623 km, KP to Mauna Kea (MK) = 4466 km, and KP to Saint Croix (SC) = 4839 km. For these longer baselines the systematic bias is greater.

Differential ionosphere strengths, converted to their effect on visibility phases at 1400 MHz, are shown as a function of time on all baselines to Kitt Peak, the reference antenna for this observation, in Figures 2, 3, and 4. The phase differences on the four shortest baselines shown (KP to FD, LA, OV, or PT) all have RMS values less than 1 radian, and are centered close to zero phase. The longer baselines often show large systematic offsets from zero phase. See for example the BR–KP and KP–MK baselines. Without correction a displacement of the pulsar from its true sky location results. The data in these figures is from the 1999 November 16, observations of PSR B1929+10. The sun was  $68^\circ$  from the pulsar during this observation. Sunset occurred at Saint Croix during the observation and is probably responsible for the rapid change in ionospheric phase delay near the end of the observation on the KP–SC baseline. Observations made when the pulsar and sun are on opposite sides of the Earth show considerably smaller ionospheric phase delays but still exhibit fluctuations on the 10 minute timescale. B1929+10 is separated from its calibrator by  $2^\circ 20'$ .

#### 4.2. Position determination

Final pulsar images were made once the ionosphere calibration was completed. A separate image was made for each 8 MHz band. The position of the pulsar was measured by fitting a Gaussian ellipse to the pulsar image. Data from a single 8 MHz spectral window produced images of the pulsar with signal-to-noise of about 40. The dominant source of the image noise was phase scatter due to the troposphere, making the final signal-to-noise ratio almost independent of the pulsar’s strength. In most cases the position agreement between images made at two different frequencies was better than 0.1 mas. A misalignment of more than this amount prompted a detailed inspection of the calibration process and usually resulted in stricter elevation limits or the removal of a frequency band with severe radio frequency interference. Once image alignment was achieved, a final image was made incorporating the data from all useful frequency bands. The final position measurement was made from this image. The synthesized beam sizes for the final images were about 10 mas north–south and 4 mas east–west but varied slightly depending on source declination.

#### 4.3. Calculation of Parallax and Proper Motion

We model the path of the pulsar in terms of its position at epoch 2000.0 ( $\alpha_{2000}, \delta_{2000}$ ), proper motion ( $\mu_\alpha, \mu_\delta$ ), and parallax ( $\pi$ ) by

$$\begin{cases} \alpha(t) &= \alpha_{2000} + \mu_\alpha t + \pi f_\alpha(\alpha_{2000}, \delta_{2000}, t) \\ \delta(t) &= \delta_{2000} + \mu_\delta t + \pi f_\delta(\alpha_{2000}, \delta_{2000}, t) \end{cases} \quad (5)$$

where  $t$  is time since year 2000.0. The functions  $f_\alpha$  and  $f_\delta$  are the parallax displacements in right ascension and declination, respectively, for an object at a distance of 1 pc as a function of the time of year. The five parameters are determined by minimizing the  $\chi^2$  function associated with the above model using an iterative linear inversion. Uncertainties in the fit parameters were based on the single-epoch position uncertainties.

## 5. Results

The proper motion and parallax results for the nine pulsars with new parallaxes are shown in Table 4. The distances to the pulsars derived from their parallax measurement are shown in comparison with their dispersion measure (DM) derived distances in Table 5. The uncertainties in DM distance are obtained by assigning the DM a Gaussian probability distribution function (PDF) centered on the measured DM with a 40% variance. The DM PDF provides a way to account for the uncertainty in the dispersion model; it is not meant to reflect uncertainty in the the dispersion measures as the DMs of the pulsars studied in this sample are measured to better than 1%. Since the dispersion model is not smooth, a non-Gaussian distance PDF is obtained when the dispersion model is applied to the Gaussian DM PDF. The most probable distance is quoted along with errors bracketing the most compact 68% likelihood region. B1237+25 has a very high  $d_{\text{DM}}$  upper limit because of its position high above the galactic plane ( $z \sim 850$  pc). The dispersion model provides poor constraints to its distance since very little ionized material is thought to be at or above this pulsar’s height. Also listed in Table 5 are the pulsars’ transverse velocities ( $v_\perp$ ) and the average electron densities ( $n_e$ ) along lines of sight.

The derived parameters of six other pulsars with accurate parallax distances are shown in Table 6. Chatterjee et al. (2001) measured the parallax of B0919+06 using the VLBA. The proximity of an in-beam calibrator to the pulsar ( $\theta_{\text{sep}} < 20'$ ), and their simultaneous observation, reduce the amount of uncalibrated ionosphere and troposphere. Further, GPS data was used to model and remove most of the remaining differential ionosphere. Single epoch uncertainties as low as 0.2 mas were attained in this manner. The other five pulsars are millisecond pulsars with distances determined through pulse arrival timing. B1534+12 has a timing parallax upper limit of  $\pi < 1.8$  mas. A more accurate distance of  $d = 1.08 \pm 0.15$  was inferred for this pulsar by monitoring the decrease in its binary period,  $\dot{P}_b$ . By assuming that General Relativity accurately predicts the orbital decay of this close neutron star binary via emission of gravitational radiation, the other contributions to  $\dot{P}_b$  from the motion of the system restricts its possible distance. (Stairs et al. 1998 & 1999).

The distances to the pulsars in Tables 5 and 6 are plotted in Figure 14. The dispersion



measure distances to these pulsars are plotted against the parallax distances in Figure 15. The dispersion measure distances tend to be smaller than the observed parallax distances. This may be due to the local low electron density bubble not being included in the dispersion measure model. For more detail on the local bubble, see Toscano et al. (1999).

Table 4. Position, Proper Motion and Parallax Results

Pulsar	$\alpha_{2000}^{\dagger}$	$\delta_{2000}$	$\mu_{\alpha}$ (mas/yr)	$\mu_{\delta}$ (mas/yr)	$\pi$ (mas)
B0329+54	03 <sup>h</sup> 32 <sup>m</sup> 59 <sup>s</sup> .3862	54°34′43″.5051	17.00 ± 0.27	−9.48 ± 0.37	0.94 ± 0.11
B0809+74	08 <sup>h</sup> 14 <sup>m</sup> 59 <sup>s</sup> .5412	74°29′05″.3671	24.02 ± 0.09	−43.96 ± 0.35	2.31 ± 0.04
B0950+08	09 <sup>h</sup> 53 <sup>m</sup> 09 <sup>s</sup> .3071	07°55′36″.1475	−2.09 ± 0.08	29.46 ± 0.07	3.82 ± 0.07
B1133+16	11 <sup>h</sup> 36 <sup>m</sup> 03 <sup>s</sup> .1829	15°51′09″.7257	−73.95 ± 0.38	368.05 ± 0.28	2.80 ± 0.16
B1237+25 <sup>‡</sup>	12 <sup>h</sup> 39 <sup>m</sup> 40 <sup>s</sup> .3589	24°53′50″.0193	−106.82 ± 0.17	49.92 ± 0.18	1.16 ± 0.08
B1929+10	19 <sup>h</sup> 32 <sup>m</sup> 13 <sup>s</sup> .9496	10°59′32″.4178	94.82 ± 0.26	43.04 ± 0.15	3.02 ± 0.09
B2016+28	20 <sup>h</sup> 18 <sup>m</sup> 03 <sup>s</sup> .8332	28°39′54″.1527	−2.64 ± 0.21	−6.17 ± 0.38	1.03 ± 0.10
B2020+28	20 <sup>h</sup> 22 <sup>m</sup> 37 <sup>s</sup> .0718	28°54′23″.0300	−4.38 ± 0.53	−23.59 ± 0.26	0.37 ± 0.12
B2021+51	20 <sup>h</sup> 22 <sup>m</sup> 49 <sup>s</sup> .8655	51°54′50″.3881	−5.23 ± 0.17	11.54 ± 0.28	0.50 ± 0.07

<sup>†</sup>A pulsar’s epoch 2000.0 position, ( $\alpha_{2000}$ ,  $\delta_{2000}$ ) is based on the position of the reference source used (see Table 3) and is accurate to about 15 mas.

<sup>‡</sup>B1237+25 data is based on its closest calibrator, J1240+2405.

Table 5. Derived parameters

Pulsar	$d_{\text{DM}}$ (kpc)	$d_{\pi}^{\dagger}$ (kpc)	$v_{\perp}$ (km s $^{-1}$ )	$n_{\text{e}}^{\ddagger}$ (cm $^{-3}$ )
B0329+54	$1.4^{+0.3}_{-0.5}$	$1.03^{+0.13}_{-0.12}$	$95^{+12}_{-11}$	$0.0253 \pm 0.0030$
B0809+74	$0.31^{+0.12}_{-0.13}$	$0.433^{+0.008}_{-0.008}$	$102^{+2}_{-2}$	$0.0133 \pm 0.0002$
B0950+08	$0.16^{+0.06}_{-0.07}$	$0.262^{+0.005}_{-0.005}$	$36.6^{+0.7}_{-0.7}$	$0.0113 \pm 0.0002$
B1133+16	$0.26^{+0.11}_{-0.11}$	$0.35^{+0.02}_{-0.02}$	$631^{+38}_{-35}$	$0.0136 \pm 0.0008$
B1237+25	$0.6^{+15.2}_{-0.5}$	$0.85^{+0.06}_{-0.06}$	$475^{+34}_{-30}$	$0.0108 \pm 0.0007$
B1929+10	$0.17^{+0.06}_{-0.07}$	$0.331^{+0.010}_{-0.010}$	$163^{+4}_{-5}$	$0.0096 \pm 0.0003$
B2016+28	$0.7^{+0.3}_{-0.3}$	$0.95^{+0.09}_{-0.09}$	$30^{+3}_{-4}$	$0.0146 \pm 0.0013$
B2020+28	$1.3^{+0.5}_{-0.5}$	$2.3^{+1.0}_{-0.6}$	$256^{+114}_{-61}$	$0.0092 \pm 0.0030$
B2021+51	$1.2^{+0.5}_{-0.5}$	$1.9^{+0.3}_{-0.2}$	$115^{+18}_{-15}$	$0.0113 \pm 0.0016$

$^{\dagger}$ Gaussian parallax uncertainties imply non-Gaussian distance uncertainties. The most compact 68% uncertainty interval is shown above.

$^{\ddagger}$ The mean electron density to the pulsar,  $n_{\text{e}}$ , is  $\text{DM } d^{-1}$ .

Table 6. Derived parameters of other pulsars with accurate distances

Pulsar	$d_{\text{DM}}$ (kpc)	$d_{\pi}$ (kpc)	$v_{\perp}$ (km s <sup>-1</sup> )	$n_{\text{e}}$ (cm <sup>-3</sup> )	Reference
J0437-4715	$0.14^{+0.05}_{-0.06}$	$0.17^{+0.03}_{-0.02}$	$109^{+17}_{-14}$	$0.0148 \pm 0.0021$	1
B0833-45	$0.61^{+1.20}_{-0.17}$	$0.28^{+0.06}_{-0.05}$	$67^{+16}_{-12}$	$0.2319 \pm 0.0477$	2
B0919+06	$6^{+13}_{-3}$	$1.15^{+0.21}_{-0.16}$	$484^{+87}_{-66}$	$0.0226 \pm 0.0036$	3
B1534+12	$0.7^{+12.0}_{-0.6}$	$1.08^{+0.16}_{-0.14}$	$131^{+20}_{-17}$	$0.0104 \pm 0.0014$	4
B1855+09	$0.7^{+0.3}_{-0.3}$	$0.79^{+0.29}_{-0.17}$	$23^{+8}_{-5}$	$0.0146 \pm 0.0040$	5
J1713+0747	$0.8^{+0.3}_{-0.3}$	$0.9^{+0.4}_{-0.2}$	$28^{+13}_{-8}$	$0.0144 \pm 0.0048$	6
J1744-1134	$0.17^{+0.06}_{-0.07}$	$0.35^{+0.03}_{-0.02}$	$35^{+2}_{-2}$	$0.0088 \pm 0.0006$	7

References. — (1) Sandhu et al., 1997; (2) Caraveo et al., 2001; (3) Chatterjee et al., 2001; (4) Stairs et al., 1999; (5) Kaspi et al., 1994; (6) Camilo et al., 1994; (7) Toscano et al., 1999

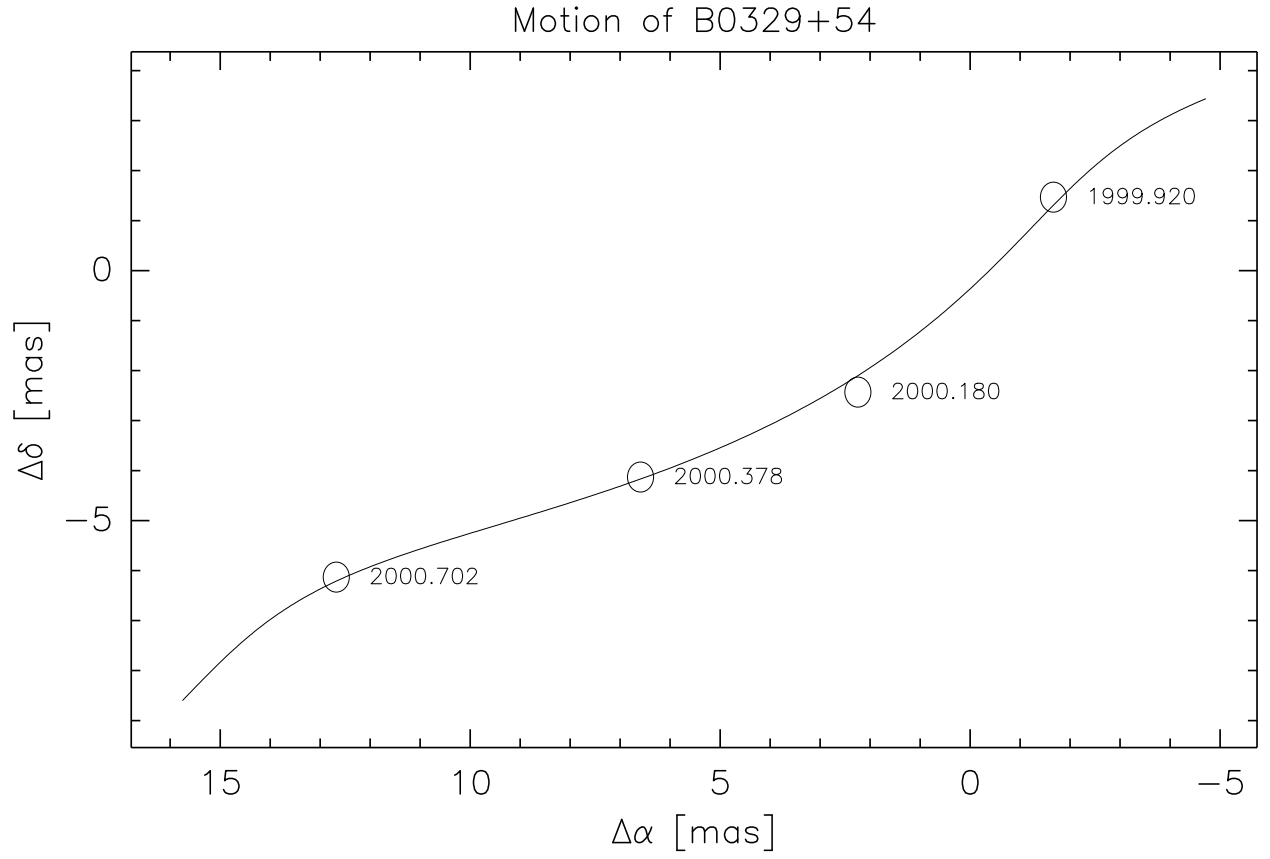


Fig. 5.— The modeled path of B0329+54 based on parameter estimates (see text) and its four measured positions. The ellipses represent  $1\sigma$  position uncertainties.

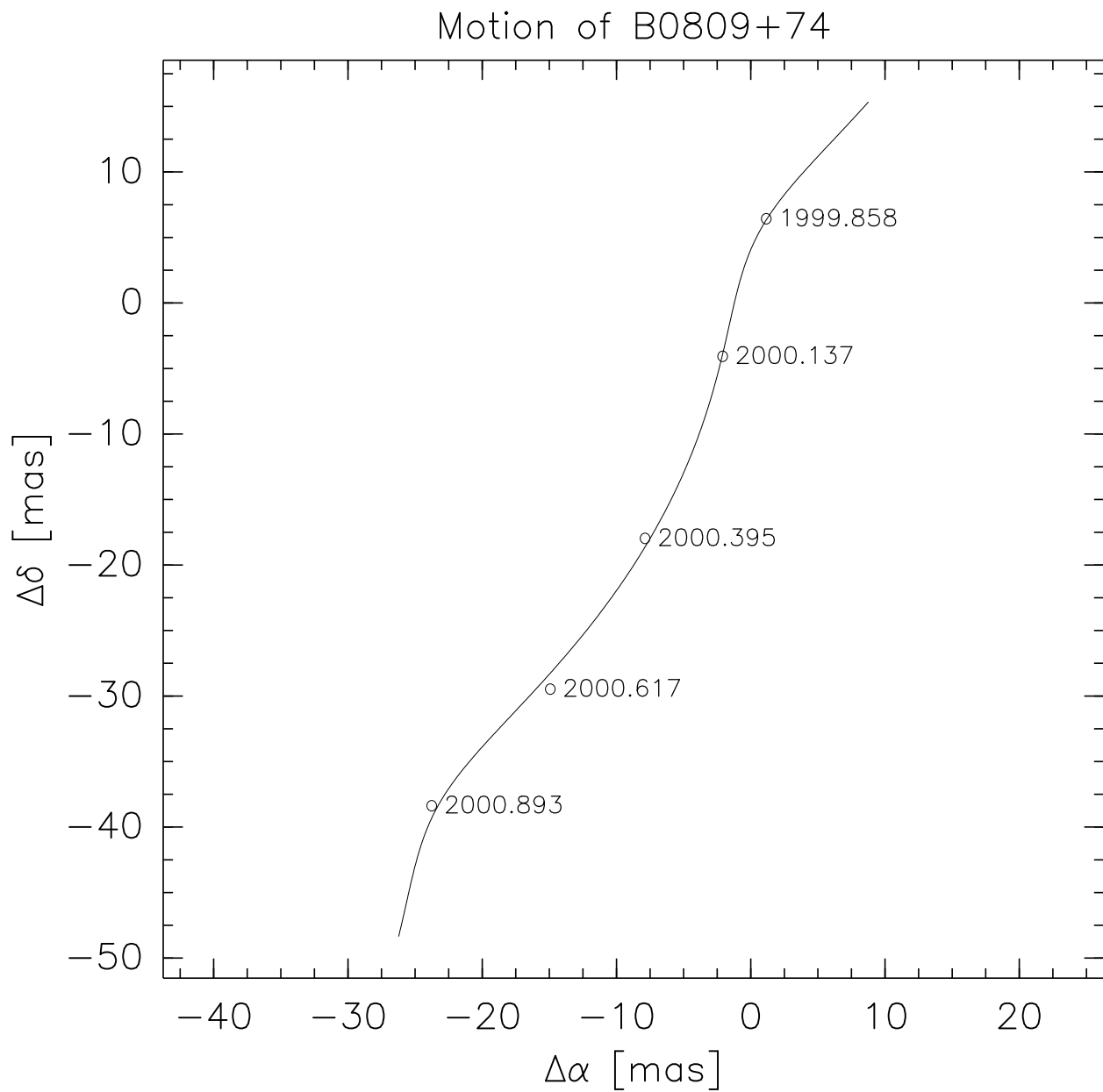


Fig. 6.— The modeled path of B0809+74 and its five measured positions.

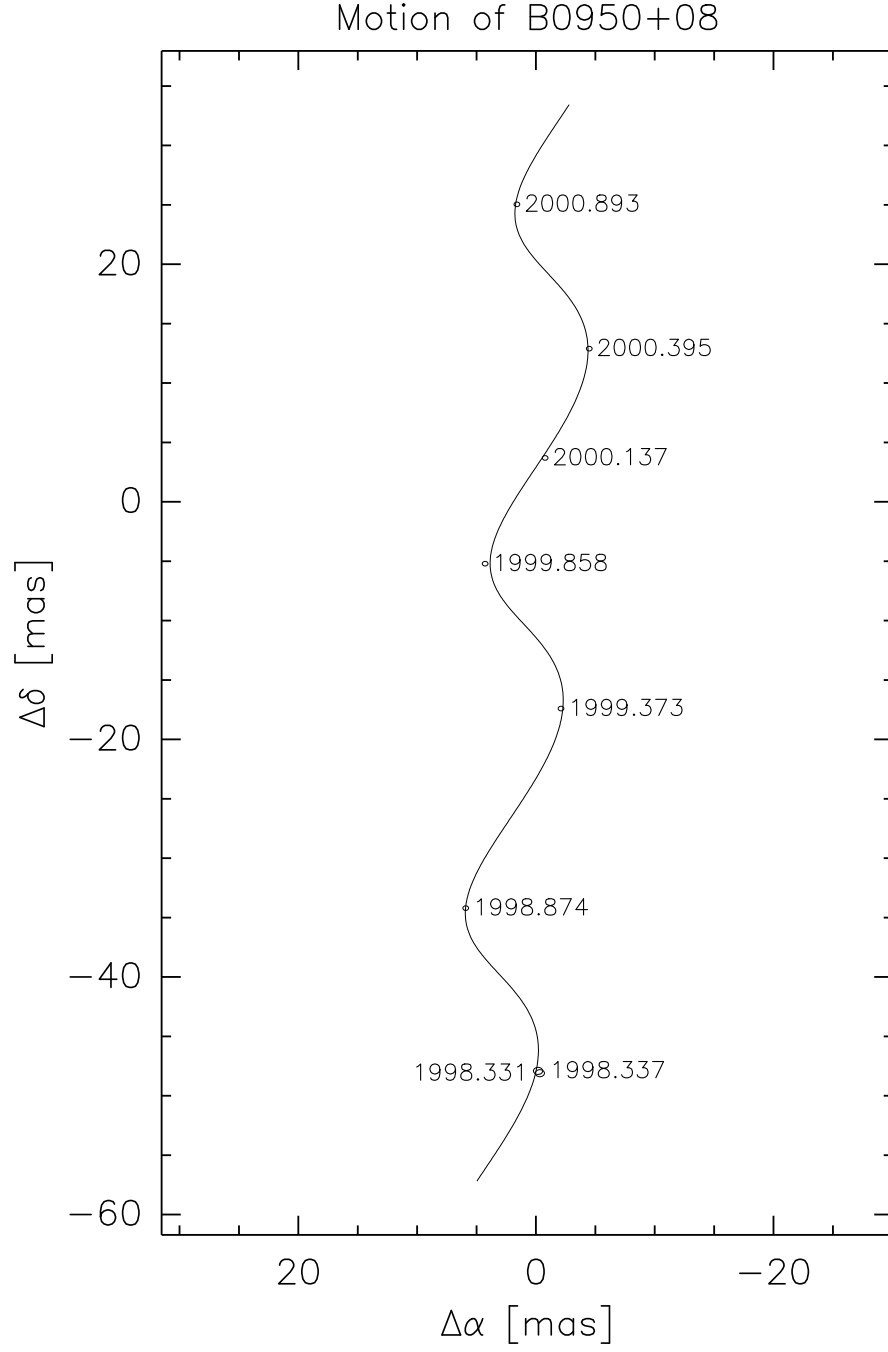


Fig. 7.— Eight observations of B0950+08 made over seven epochs and its modeled path.

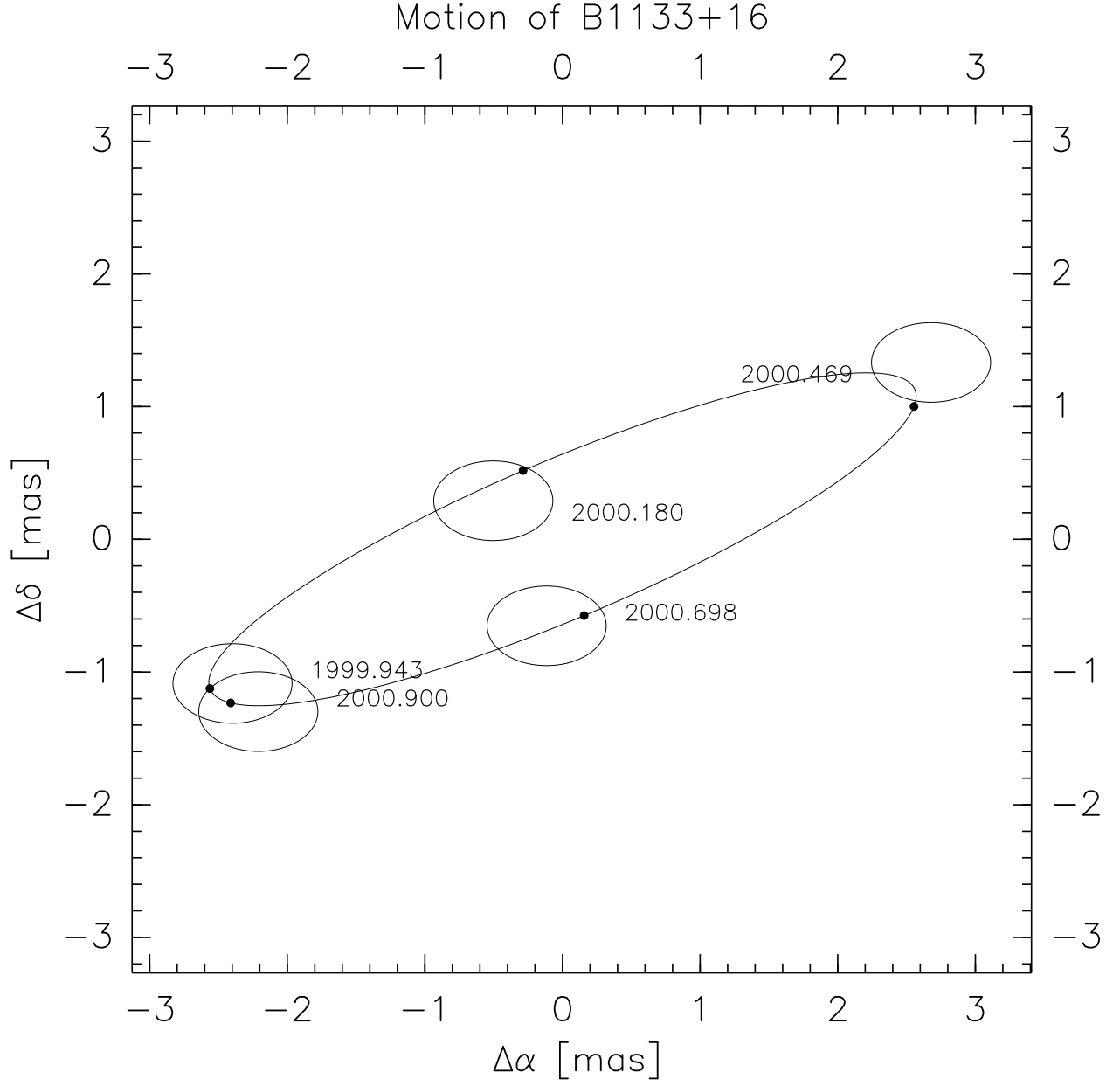


Fig. 8.— A plot showing the measured positions of B1133+16 at 5 epochs and its modeled path, both with the estimated proper motion removed. This pulsar’s proper motion of  $375 \text{ mas yr}^{-1}$  ranks as one of the highest. The proper motion was subtracted to allow the significance of the parallax to be visible.



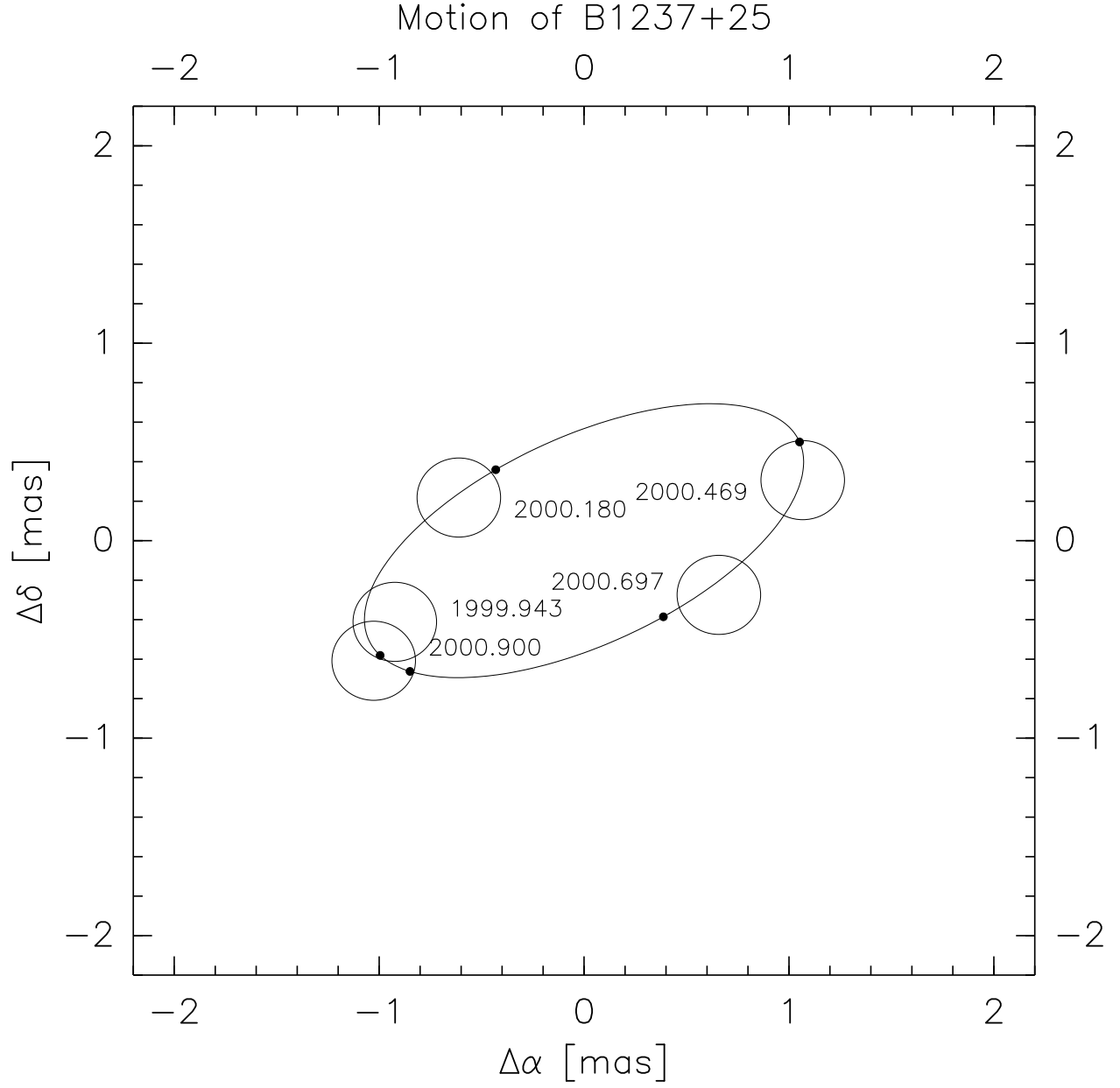


Fig. 9.— A plot showing the measured positions of pulsar B1237+25 at 5 epochs and its modeled path, both with the estimated proper motion removed. The linear motion of this pulsar moves it 118 mas each year.

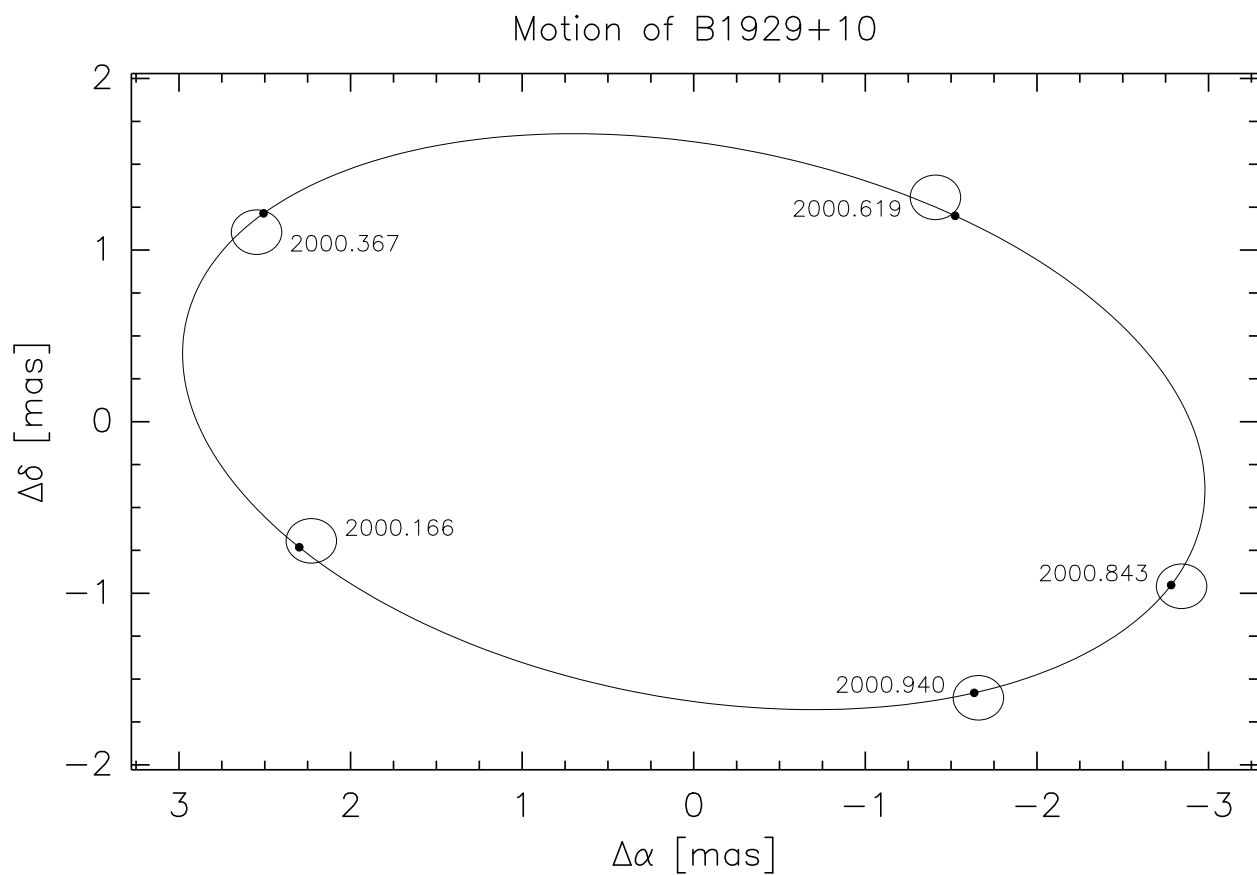


Fig. 10.— A plot showing the measured positions of B1929+10 at 5 epochs and its modeled path, both with the estimated proper motion removed. The proper motion was subtracted before plotting since its linear motion over one year amounts to 104 mas.

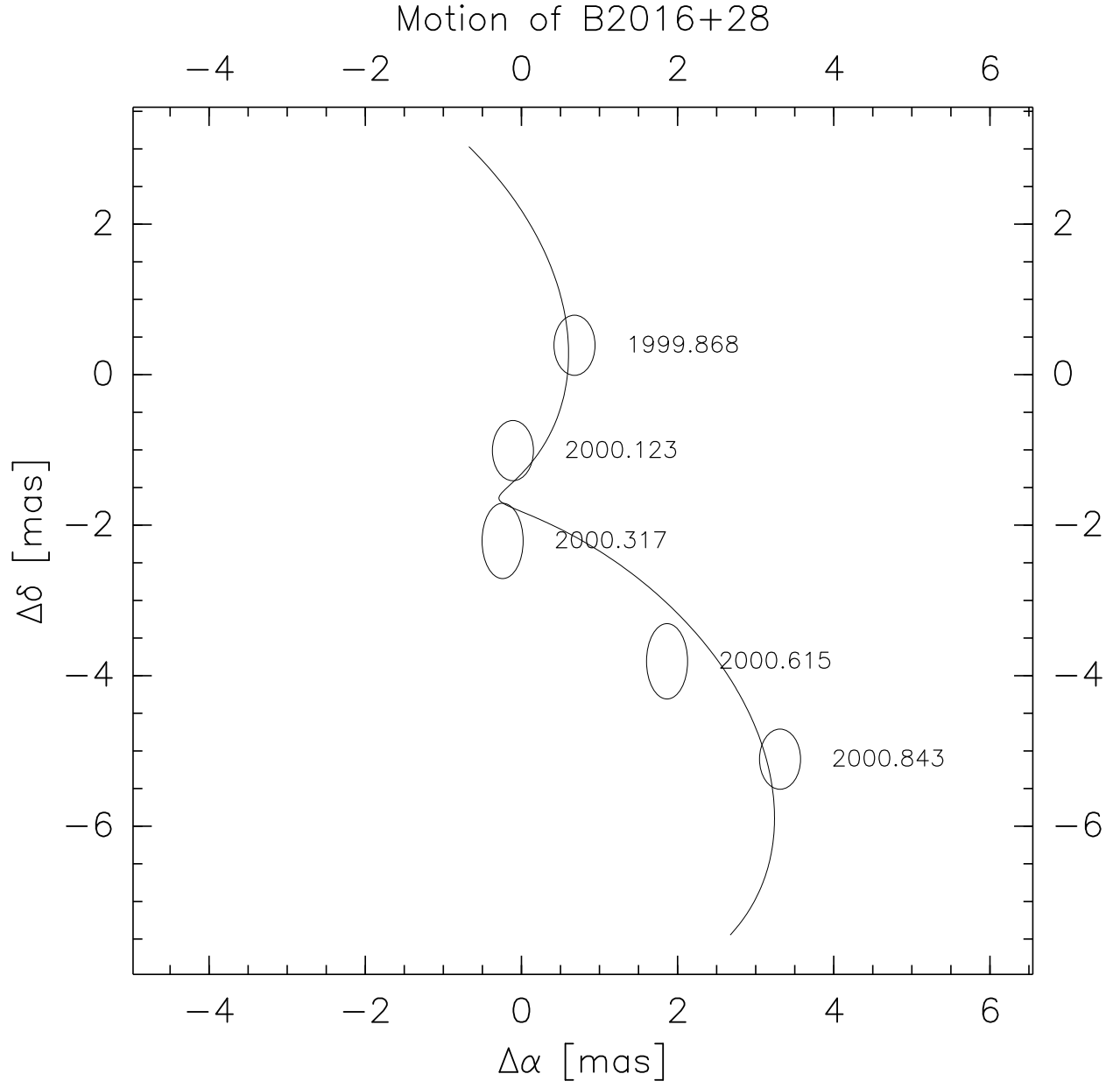


Fig. 11.— The modeled path of B2016+28 and its five measured positions.

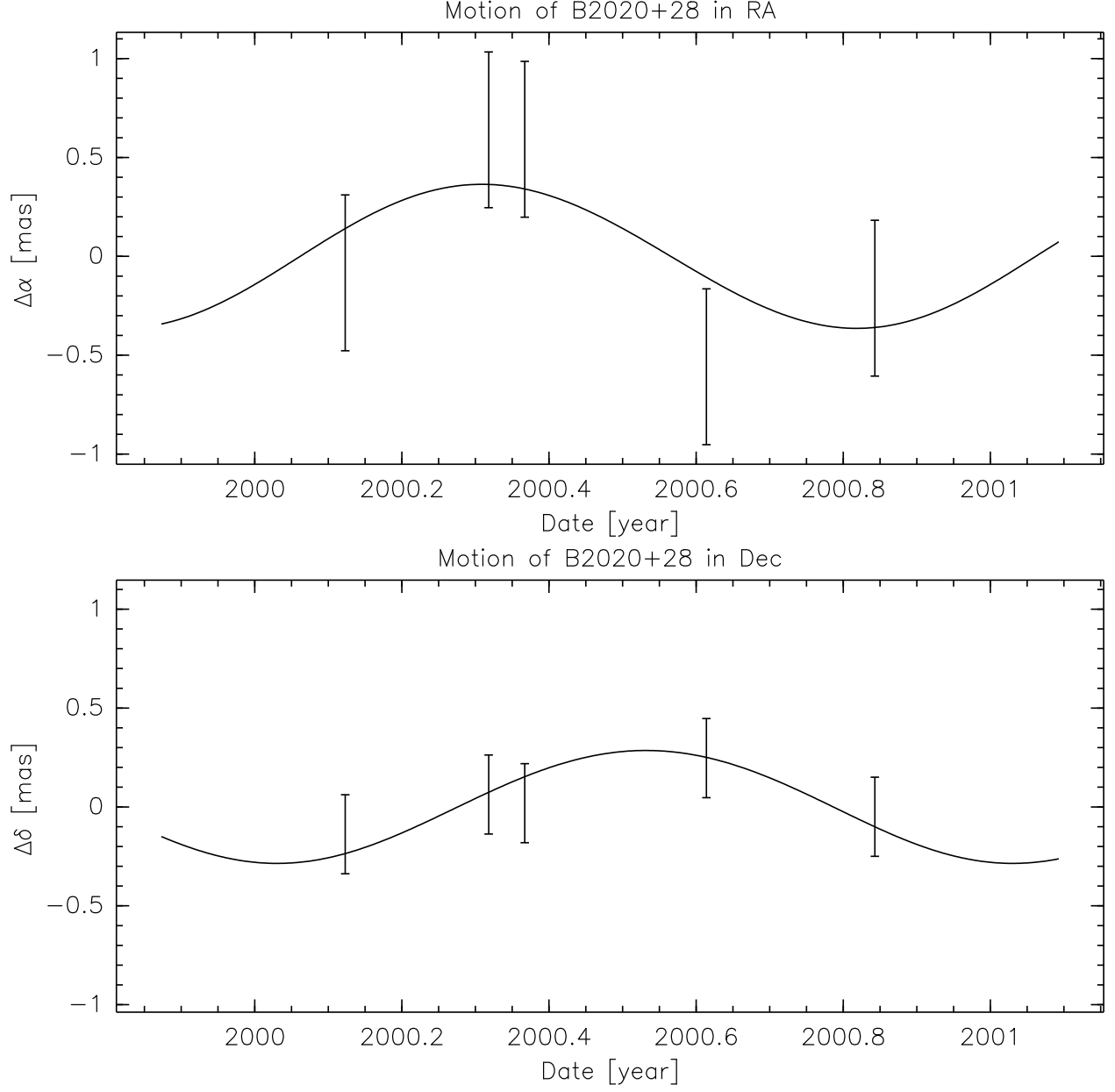


Fig. 12.— The large distance to B2020+28 makes its parallax measurement the smallest of those observed. Its parallax fit is shown above with its proper motion subtracted. Because this pulsar’s single-epoch position measurements are comparable in magnitude to the estimated parallax, the parallax fit is better visualized one dimension at a time.

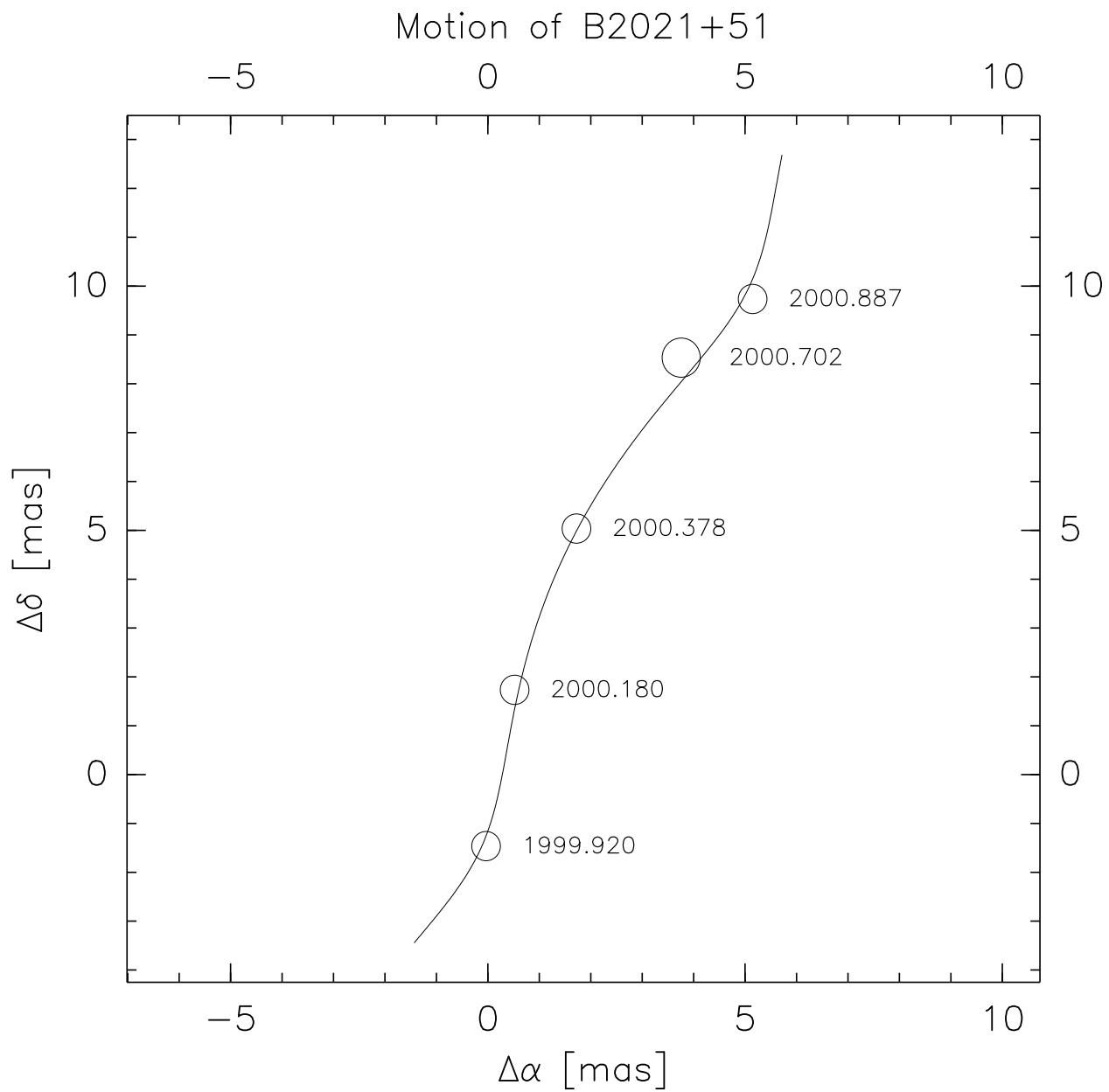


Fig. 13.— The modeled path of B2021+51 and its five position measurements.

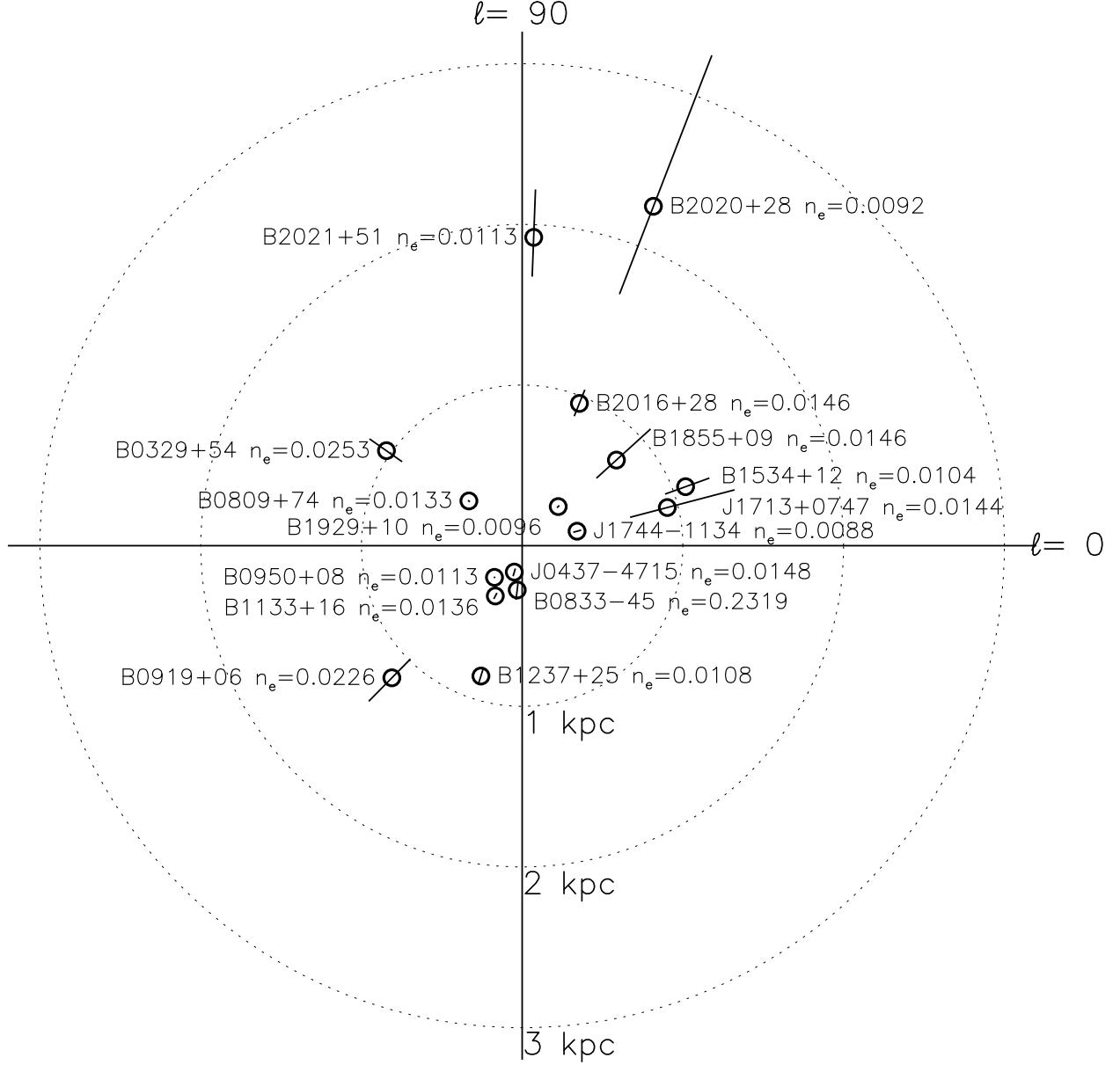


Fig. 14.— A projection of pulsars with accurate distance measurements onto the galactic plane. Each pulsar is labeled with its name and estimated line of sight electron density,  $n_e$ . The radial line through each pulsar is its distance error bar, representing its most compact 68% confidence interval.

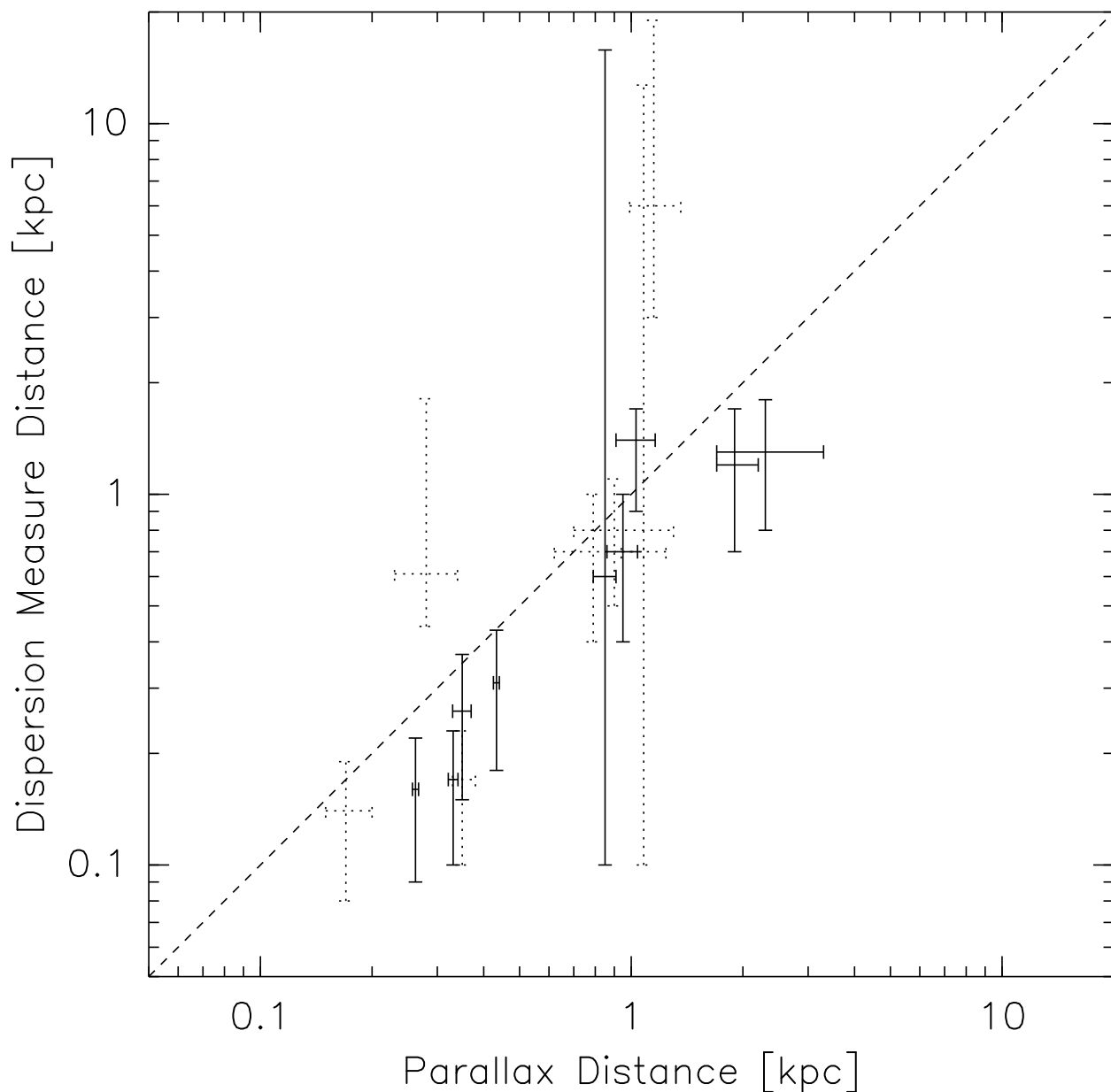


Fig. 15.— Dispersion measure derived distances compared against parallax distances. The solid error bars are for the nine pulsars studied in this work (listed in Table 5); the dotted error bars are for those pulsars in Table 6. Error bars in each dimension represent the most compact 68% confidence interval. The predominance of pulsars to the lower right of the dashed diagonal line suggest that the dispersion model systematically underestimates distances to nearby pulsars.

## 6. Uncertainties and Limitations

Several error estimators were used to set the final parallax errors. Pulsar images made at each of the 8 MHz bands were fit for position. In almost all cases scatter in position was about 0.1 mas or less. For the brightest pulsars this scatter in position dominated the final uncertainty. The other single-epoch consistency check was making images at several different short time ranges ( $\sim 30$  minutes) and observing the apparent motion of the pulsar over the  $\sim 2.5$  hours of its observation. The dominant motion was always in right ascension, never amounting to more than 0.3 mas. Excising low elevation data ( $< 20^\circ$ ) usually reduced this disagreement to less than 0.1 mas. The source of this wander is almost certainly differential refraction in the troposphere and its effect scales with calibrator-target separation at approximately 0.05 mas per degree of separation, although it is very likely that the scaling is non-linear for separations larger than those probed with these observations. Based on the tropospheric limitations, calibrator separations greater than the  $5^\circ$  limit that was initially set would probably not generate single-epoch position measurements with accuracies better than about 0.3 mas. While station weather data was used to estimate tropospheric refraction, more sophisticated tropospheric modeling techniques exist and should be employed in future observations. Correlator model deficiencies, such as incorrect Earth orientation or station positions or calibrator positions, can also cause relative motion between the target and calibrator. The success of geodesy experiments at the  $10 \mu\text{as}$  level using the same correlator model as was used for this work suggest that these effects are not significant for these observations. The post-fit residuals provide the final check on the uncertainties. The least squares fit quality parameter,  $\chi^2/(2N_{\text{epochs}} - 5)$ , was less than 1.5 for all nine pulsars, indicating that the single epoch error estimates are reasonable.

Pulsar B1237+25 offered a unique test of the final uncertainties. The pulsar and two calibrators were observed together in a slightly longer three-pointing nodding cycle. This allowed the relative proper motions and parallaxes of each pair to be measured. Table 7 shows the proper motions and parallaxes measured for each pair, which are in excellent agreement.

The small calibrator-to-pulsar separation is not the only limitation to the ionosphere calibration. The fitting of the phases imposes sensitivity requirements. Phase solutions accurate to  $\sim 10^\circ$  are required on timescales of 30 seconds or less for each frequency band.

B0950+08 now has seven epochs of VLBA astrometric data spanning just over 2.5 years. Figure 7 shows these measurements and its estimated proper motion and parallax. The RMS fit residual in right ascension was 0.22 mas, and that in declination was 0.15 mas, similar to the uncertainty estimated by its single-epoch position uncertainties, typically 0.2 mas. Its distance,  $262 \pm 5$  parsecs, is the most accurate pulsar distance measurement made to date.



Table 7. Calibration Consistency Test

Calibrator	Target	$\mu_\alpha$ (mas yr <sup>-1</sup> )	$\mu_\delta$ (mas yr <sup>-1</sup> )	$\pi$ (mas)
J1240+2405	B1237+25	$-106.82 \pm 0.17$	$49.92 \pm 0.18$	$1.16 \pm 0.08$
J1230+2518	B1237+25	$-106.53 \pm 0.24$	$50.21 \pm 0.23$	$1.08 \pm 0.11$
J1240+2405	J1230+2518	$0.10 \pm 0.23$	$0.09 \pm 0.19$	$0.13 \pm 0.11$

## 7. Conclusions

The ionosphere calibration method used in this paper successfully removed the effect of the ionosphere from the VLBA data for all nine detected pulsars, allowing sub-milliarcsecond parallax measurements to be made. The requirements for this technique to work can be easily summarized – station-based phases must be measurable to  $\sim 10^\circ$  at each frequency band with 30 second or shorter solution intervals. For our observations, the limiting flux density at 1400 MHz is about 8 mJy. Observing with a larger bandwidth, dividing the bandwidth into fewer spectral windows, or adding larger VLBI stations to the array would allow this technique to operate on weaker pulsars. Up to 100 more pulsar parallaxes are within reach of the VLBA.

The pulsar timing data used for gating the correlator was very kindly provided by Andrew Lyne of Jodrell Bank Observatory. The National Radio Astronomy Observatory is a facility of the National Science Foundation operated under cooperative agreement by Associated Universities, Inc. A National Science Foundation graduate student fellowship funded Walter Bricken. Additional funding was provided by Princeton University and by the NSF (AST-0098343).

## REFERENCES

- Backer, D. C. & Sramek, R. A. 1982, *ApJ*, 260, 512.
- Bailes, M., Manchester, R. N., Kesteven, M. J., Norris, R. P. & Reynolds, J. E. 1990, *Nature*, 343, 240.
- Beasley, A. J., Gordon, D., Peck, A. B., Petrov, L., MacMillan, D. S., Fomalont, E. B. & Ma, C. 2002, *ApJS* (accepted).
- Briskin, W. F., Benson, J. M., Beasley, A. J., Fomalont, E. B., Goss, W. M. & Thorsett, S. E. 2000, *ApJ*, 541, 959.
- Briskin, W. F., Fruchter, A. S., Goldberg, E. E., Goss, W. M., McGary, R. S., & Thorsett, S. E. (in prep).
- Camilo, F., Foster, R. S., & Wolszczan, A. 1994, *ApJ*, 437L, 39.
- Campbell, R. M., Bartel, N., Shapiro, I. I., Ratner, M. I., Cappallo, R. J., Whitney, A. R. & Putnam, N. 1996, *ApJ*, 461, 95L.
- Caraveo, P. A., Bignami, G. F., Mignani, R., & Taff, L. G. 1996, *ApJ*, 461, 91L.
- Caraveo, P. A., De Luca, A., Mignani, R. P., & Bignami, G. F. 2001, *ApJ*, 561, 930
- Chatterjee, S., Cordes, J. M., Goss, W. M., Fomalont, E. B., Beasley, A. J., Lazio, T. J. W., & Arzoumanian, Z. 2001, *ApJ*, 550, 287.
- Gwinn, C. R., Taylor, J. H., Weisberg, J. M., & Rawley, L.A. 1986, *AJ*, 91, 338.
- Kaspi, V. M., Taylor, J. H. & Ryba, M. F. 1994, *ApJ*, 428, 713.
- Salter, M. J., Lyne, A. G., & Anderson, B. 1979, *Nature*, 280, 477.
- Sandhu, J. S., Bailes, M., Manchester, R. N., Navarro, J., Kulkarni, S. R. & Anderson, S. B. 1997, *ApJ*, 478, 95L.
- Sfeir, D. M., Lallement, R., Crifo, F. & Welsh, B. Y. 1999, *A&A*, 346, 785.
- Shapiro, I. I., Wittels, J. J., Counselman, C. C., III, Robertson, D. S., Whitney, A. R., Hinteregger, H. F., Knight, C. A., Clark, T. A., Hutton, L. K. & Niell, A. E. 1979, *AJ*, 84, 1459.
- Stairs, I. H., Arzoumanian, Z., Camilo, F., Lyne, A. G., Nice, D. J., Taylor, J. H., Thorsett, S. E., & Wolszczan, A. 1998, *ApJ*, 505, 352.

- Stairs, I. H., Nice, D. J., Thorset, S. E. & Taylor, J. H. 1999, Gravitational Waves and Experimental Gravity, XXXIV Rencontres de Moriond.
- Taylor, J. H., Cordes, J. M. 1993, ApJ, 411, 674.
- Taylor, J. H., Manchester, R. N., & Lyne, A. G. 1993, ApJS 88, 529.
- Synthesis Imaging in Radio Astronomy II, Taylor, G. B., Carilli, C. L., & Perley, R. A., 1998, ASP Conference Series, Vol. 180. 1999.
- Toscano, M., Britton, M. C., Manchester, R. N., Bailes, M., Sandhu, S. R., Kulkarni, S. R. & Anderson, S. B. 1999, ApJL, 523, 171.
- Walter, F. M. 2001, ApJ, 549, 433.
- Weisberg, J. M., Rankin, J., & Boriakoff, V. 1980, A&A, 88, 84.